Journal of Applied Fluid Mechanics, Vol. 15, No. 6, pp. 1933-1945, 2022.
Available online at www.jafmonline.net, ISSN 1735-3572, EISSN 1735-3645.
https://doi.org/10.47176/jafm.15.06.1189

Numerical Analysis of the Effect of Streamlined Nose Length on Slipstream of High-Speed Train Passing through a Tunnel

Z. Wu [1], D. Zhou [2,3,4], S. Li [2,3,4], J. Yang [5], G. Chen [2,3,4] and X. Li [2,3,4†]

[1] *Sichuan Provincial Railway Industry Investment Group Co., Ltd., Chengdu, Sichuan 610081, China*
[2] *Key Laboratory of Traffic Safety on Track (Central South University), Ministry of Education, Changsha, Hunan 410075, China*
[3] *Joint International Research Laboratory of Key Technology for Rail Traffic Safety, Changsha, Hunan 410075, China*
[4] *National & Local Joint Engineering Research Center of Safety Technology for Rail Vehicle, Changsha, Hunan 410075, China*
[5] *China Railway Eryuan Engineering Group Co., Ltd., Chengdu, Sichuan 610031, China*

† *Corresponding Author Email: lixiaofangabm@126.com*

(Received March 18, 2022; accepted June 28, 2022)

ABSTRACT

The improved delayed detached eddy simulation (IDDES) method was employed based on the shear–stress transport (SST) κ-ω two-equation turbulence model to simulate the slipstream distribution characteristics of a high-speed train traversing a tunnel. The accuracy of the numerical simulation method was verified through a full-scale test. First, the wake vortex structure and the distribution of slipstreams of the train with a streamlined nose length of 7 m running in a tunnel were analyzed. Then, the influence of the streamlined nose length on the wake dynamics and slipstream was compared and analyzed. The slipstream positive peak decreased with increasing distance from the top of the rail and center of the track. As the streamlined nose length increases, the vortex intensity in the wake area weakens; moreover, the influence ranges of the wake vortex and the slipstream positive peak value become smaller. Compared with the results of a train having a streamlined nose length of 5 m, the slipstream positive peak value at 1.4 m from the top of the rail and 100 m from the tunnel entrance decreased by 46.6% from that of a train with a streamlined nose length of 9 m.

Keywords: High-speed train; Tunnel; Nose length; Slipstream; Wake dynamics.

NOMENCLATURE

H	height of the train	U, V, W	longitudinal, transverse, and vertical components of the non-dimensional slipstream velocities
$Ltu, crit$	most unfavorable tunnel length		
Ltr	length of the train		
u, v, w	longitudinal, transverse, and vertical components of the slipstream velocities	$Vtrain$	train speed
		U_R	non-dimensional resultant slipstream velocity

1. INTRODUCTION

When designing the shape of a train, the nose shape requires special consideration as it significantly influences the aerodynamic performance of the train, including the pressure wave of the train's crossing, slipstream, and aerodynamic force and transient flow structure around the train (Bell *et al*. 2017; Chen *et al*. 2017; Krajnović 2009). Therefore, the optimization of the train nose shape is an effective measure

for improving the aerodynamic performance of trains (Chen *et al*. 2018; Niu *et al*. 2018). Extensive research has been conducted to investigate the effects of the nose shape of a train on its aerodynamic characteristics (Meng *et al*. 2022, 2021b; Xie *et al*. 2019).

The biggest challenge in aerodynamic shape optimization of high-speed trains is to find the best aerodynamic shape that meets the design specifications of the train. Hence, the aerodynamic shape optimization of trains has been extensively studied. Particularly, Hemida and Krajnović (2010, 2008) analyzed the influence of nose shape on the time-averaged and instantaneous flow field around the train and the aerodynamic force of the train under crosswind using large-eddy simulation. The results showed that the vortex structure in the wake area of a short nose is greater than that of a long one, affecting the main frequency caused by shear layer instabilities. The mean and standard deviation of the aerodynamic drag and lift force and the slipstream velocity decreased as the nose streamlined length increased. Moreover, the boundary layer distribution and wake dynamics are severely modified by the nose streamlined length (Chen *et al*. 2019; Li *et al*. 2019). Tian *et al*. (2006) and Zhang and Zhou (2013) studied the influence of the train nose streamlined length, width, and height on the pressure wave and aerodynamic force of trains crossing. A series of theoretical relations between the nose shape parameters of the train and its aerodynamic performance was established, and the results were applied to the streamlining design of a high-speed train. Many scholars have adopted optimization algorithms to optimize the aerodynamic shape of the train nose and improve the efficiency of train nose shape optimization (Munoz-Paniagua *et al*. 2015; Yao *et al*. 2014, 2016). To explore the relationship between train shape design parameters and the aerodynamic force, Li *et al*. (2016) used a multi-objective optimization algorithm to optimize the aerodynamic shape of a train, and find the train shape with the best aerodynamic performance. Kwak *et al*. (2013) established a three-dimensional control function for the train nose, investigated the influence of the cross-sectional shape of the train nose on the aerodynamic resistance of the train using the Broyden–Fletcher–Goldfarb–Shanno algorithm, and obtained a train nose shape that could reduce the aerodynamic resistance by 23%. Muñoz-Paniagua *et al*. (2012) and Paniagua *et al*. (2011) used a combination of genetic algorithms, metamodels, and artificial neural networks to optimize the nose shape and reduce the aerodynamic drag of high-speed trains. They also provided a schematic diagram of the optimization process and introduced the most relevant elements in detail. The aforementioned studies show that a better train nose shape can effectively improve the aerodynamic performance of trains running in open air.

However, the aerodynamic characteristics of trains in tunnels are different from those of trains running in open air (Gilbert *et al*. 2013; Jiang *et al*. 2019; Wang *et al*. 2022). Because of the tunnel space limitations, when a high-speed train passes through a tunnel, aerodynamic effects such as alternating pressure and slipstream will have greater impacts on passenger comfort, safety of people beside the track, service life of auxiliary facilities in the tunnel, and stability of train operation compared to running in open air. There are various measures to alleviate train–tunnel aerodynamic effects, and a reasonable train streamline design is one of the most effective methods (Meng *et al*. 2021a; Yoon *et al*. 2001). For example, the aerodynamic resistance of the train in a tunnel is reduced by approximately 50% if the shape of the train nose is changed from blunt to streamlined (Choi and Kim 2014). Munoz-Paniagua *et al*. (2012) and Paniagua *et al*. (2011) not only optimized the train nose shape to reduce aerodynamic drag in the open air but also applied a genetic algorithm and numerical simulation method to the nose shape optimization of a high-speed train in a tunnel to minimize the pressure gradient of the compression wave and aerodynamic resistance of the train (Muñoz-Paniagua *et al*. 2014). Doi *et al*. (2010) measured the pressure wave of a train traversing a tunnel with a 1/30 scale moving model test device and analyzed the influence of the nose shape of the train on the strength and form of the pressure wave. Miyachi *et al*. (2016) investigated the effect of train nose shape on the compression wave and micro-pressure wave of a tunnel using a moving model test. The results showed that the maximum pressure gradient of the compression wave caused by a cone-nose train was the highest and that of a paraboloid-nose train was the lowest. Ito (2000) conducted detailed research on the aerodynamic shape of a Japanese Shinkansen train and improved the riding comfort of the train passing through a tunnel by aerodynamic shape optimization. Lee *et al*. used an optimization algorithm to optimize the train nose shape. The mechanism of the influence of a change in the nose section on the aerodynamic performance of a train was analyzed, and the nose shape that was most conducive to reducing the micro-pressure wave intensity was determined (Ku *et al*. 2010; Lee and Kim 2008, 2007). Kwon *et al*. (2001) optimized the nose shape of a high-speed train using a response surface methodology to reduce the intensity of the compression wave gradient at the tunnel entrance. At present, studies on the effect of train nose shape on train–tunnel aerodynamic effect focus on reducing aerodynamic drag and alleviating the gradient of the compression wave or intensity of the micro-pressure wave.

However, most previous studies focused on the effect of the nose streamlined length on the wake dynamics and slipstream around the train in the open air. When a train runs within a tunnel, the restrictive effect of the tunnel walls will drastically change the wake dynamics and slipstream around the train. Only a few studies have investigated this effect. According to previous studies, the wake flow generated by a train causes the slipstream velocity to greatly fluctuate (Bell *et al*. 2015). In addition, the slipstream has adverse effects on trackside personnel and facilities (Flynn *et al*. 2016; Rocchi *et al*. 2018; Xu *et al*. 2020). Therefore, it is necessary to study the influence of the train nose streamlined length on the slipstream and wake vortex structure in a tunnel; it will help in reducing the adverse effects of the slipstream on people and auxiliary facilities beside the track.

The effect of train nose streamlined length on the

wake flow dynamics and slipstream when a high-speed train runs through a tunnel is investigated using the improved delayed detached eddy simulation (IDDES) combined with the overset mesh method. First, the space–time evolution characteristics of the wake flow dynamics of the train and variation of the slipstream in the tunnel are analyzed. Subsequently, the influence of the train nose streamlined length on the slipstream and wake vortex structure of the train were compared and analyzed.

2. NUMERICAL METHOD

2.1 Computational Model

In this study, a 1/10th scale model of a train with head and tail cars of 6.64*H* and a middle car of 6.46*H* was adopted, where the scaled height *H* of the train was the characteristic length, and the scaled width *W* of the train was 0.83*H*. This study aims to explore the influence of the nose streamlined length of a high-speed train on its aerodynamics as it passes through a tunnel. Therefore, the train model was simplified, and the bogie, windshield, and pantograph structures were ignored. Figure 1(a) shows the simplified train model. Three train nose streamlined lengths (i.e., 5, 7, and 9 m) were selected for this study, as shown in Fig. 1(b).

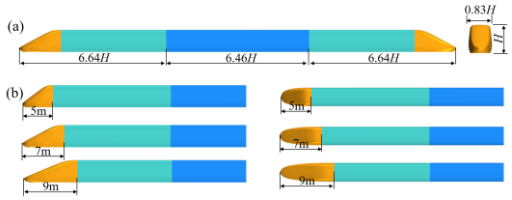

Fig. 1. Train model: (a) entire model and (b) side and top views.

2.2 Numerical Method

The commercial STAR-CCM+ 14.02.012 software was adopted to model the complete process of a high-speed train passing through a tunnel. The IDDES method based on the SST k-ω two-equation turbulence model combined with the overset mesh method was adopted to simulate the complex three-dimensional, compressible, and unsteady turbulent flow caused by the train running in the tunnel to investigate and analyze the effect of the streamline length of a train on the wake flow and slipstream distribution characteristics when a high-speed train passes through a tunnel. The implicit format with second-order accuracy was utilized to deal with time items, and the physical time step was set to 0.0001 s. In addition, although the Mach number of the train speed in the numerical simulation was less than 0.3, the pressure in the tunnel was highly unsteady due to the propagation and superposition of the pressure waves generated by the train passing through it. Therefore, the compressibility of air must be considered in the train–tunnel coupling aerodynamic simulation. All calculations were completed on the Sunway TaihuLight supercomputing platform of the National Supercomputer Center in Wuxi.

2.3 Computational Domain and Boundary Conditions

Figure 2 shows the computational domain and boundary conditions of this study. The computational domain is composed of three subzones. Zone 1 is the overset region, where the boundaries were set as overset boundary conditions and the train surfaces are set as no-slip wall boundary conditions. The cross-sectional size of zone 1 is shown in Fig. 2(b), and the size of zone 1 was set as 40*H* (length) × 1.8*H* (width) × 1.7*H* (height). The initial position of the tip of the nose of the head train was 50 m away from the entrance of the tunnel. Zone 2 is the tunnel region and it extends into the open-air region, and the tunnel surface is set as a no-slip wall. The cross-sectional zone of the full-scale tunnel is 70 m^2, and the length of the tunnel is 300.4 m, which is calculated using Eq. (1); the equation is from the CEN European Standard (2010). The calculation formula for the most unfavorable tunnel length is expressed as

$$L_{tu,crit} \approx \left(\frac{L_{tr}}{4}\right)\left(\frac{c}{V_{train}}\right)\left(1+\frac{c}{V_{train}}\right), \quad (1)$$

where V_{train} is the train speed ($V_{train} = 97.22$ m/s), c is the local speed of sound ($c = 340$ m/s), L_{tr} is the train length, and $L_{tu,crit}$ is the most unfavorable tunnel length.

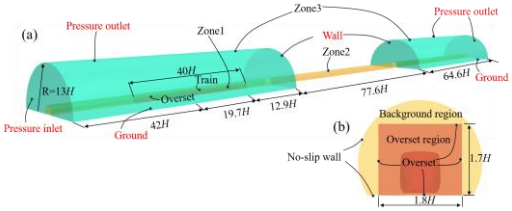

Fig. 2. Computational domain and boundary conditions: (a) overall view and (b) cross-section of the background and overset regions.

Zone 3 is composed of two open-air regions, which have identical dimensions. The two open-air regions are sufficiently large to avoid the effect of the boundary condition on the flow field within the computational domain. The pressure inlet boundary condition was applied to the left side of the left air region, and the pressure outlet boundary condition was adopted on the right side of the right air region and top of the two air regions. The other surfaces were set as no-slip wall boundary conditions.

2.4 Computational Mesh and Monitoring Points

At present, numerical simulation technologies that can realize the relative motion between train and tunnel include sliding mesh, dynamic mesh, and overset grid technologies. However, sliding mesh technology is disadvantageous because the flow field on the exchange surface is not sufficiently continuous. Dynamic mesh technology has a slow self-checking speed of grid reconstruction in the later stages of calculation. Conversely, overset mesh technology has

an excellent performance in mesh coupling and is widely used in the simulation of aerodynamic characteristics of high-speed trains and wind turbines (Chen *et al*. 2021b, 2021a, 2022; Liang *et al*. 2020; Liang *et al*. 2020; Liu *et al*. 2020). In this study, the overset mesh technology was adopted to simulate the relative movement between the train and tunnel. In a certain timestep, if the calculation converged, the overset mesh zone continued to move forward and re-assembled the grid according to the movement speed and time step, and the flow field information in the next time step was calculated until the overset mesh movement reached the preset maximum time.

Figure 3 shows a diagram of the numerical calculation grid (medium grid) used in this study. The mesh near the train surface and the wake region was refined to accurately resolve the flow separation and the vortex structures. On the surface of the train, 20 prism layers that change at a growth rate of 1.15 were added. Figure 4 shows that the y+ on the surface of the train is between 0.5 and 3. The y+ in most zones is less than 2, and only the y+ in the local zone of the head and tail cars is close to 3. The grid of the train surface and volume grid in the calculation domain are 0.013*H* and 0.026*H*, respectively. The total number of cells in the medium grid is approximately 32 million, of which the numbers of grids in the overset and background zones are 17 and 15 million, respectively.

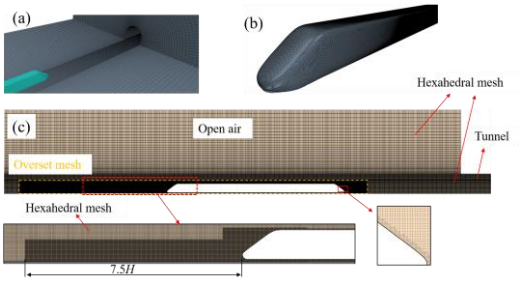

Fig. 3. Medium grid distribution: (a) tunnel entrance grid, (b) train surface grid, and (c) refined grid around the train.

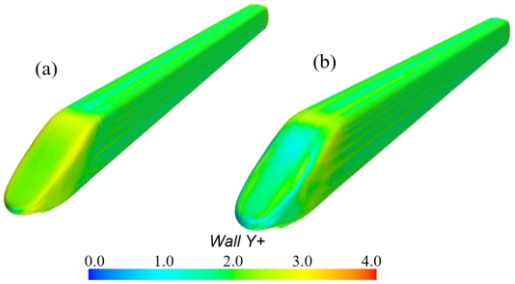

Fig. 4. Distribution of y+ (medium grid): (a) head car and (b) tail car.

To investigate the influence of mesh resolution on the numerical results, three different scale grids (i.e., coarse, medium, and fine) were generated, which had approximately 22, 32, and 45 million, respectively. Figure 5 shows the three types of grid distribution, and Fig. 6 presents a slipstream comparison of the three grid types. In addition to the reasonable deviation in the wake area, the slipstream peaks obtained by medium and fine grids show good consistency, and the difference in peak values is less than 5%. As the characteristics of the wake flow field when the high-speed train passes through the tunnel are also a primary focus of this study, Fig. 7 presents an iso-surface plot of the Q criterion of the wake region under the three grids. Based on the figure, the fine and medium grids capture the small-scale vortex structure in the wake flow more carefully than the coarse grid, and the difference between the small-scale vortex structure captured using the medium and fine grids is small. Therefore, for the wake structure and slipstream simulated in this study, the medium-scale grid generation strategy was chosen to discretize the computing domain as it can meet the requirements of calculation accuracy while being computationally less expensive than the other grid strategies.

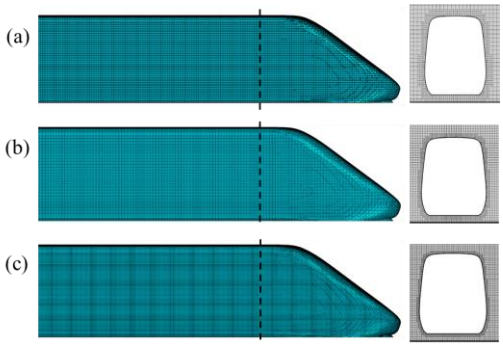

Fig. 5. Three different types of grids: (a) coarse, (b) medium, and (c) fine grids.

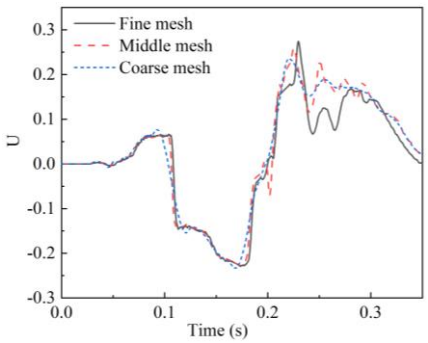

Fig. 6. Comparison of slipstreams for different mesh sizes.

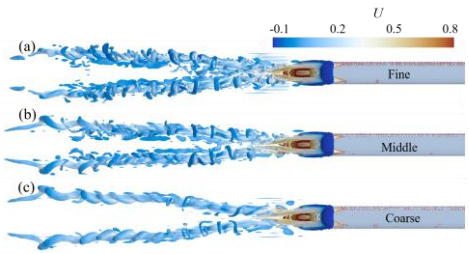

Fig. 7. Comparison of instantaneous iso-surface plot of Q criterion (Q = 20,000): (a) coarse, (b) medium, and (c) fine grids.

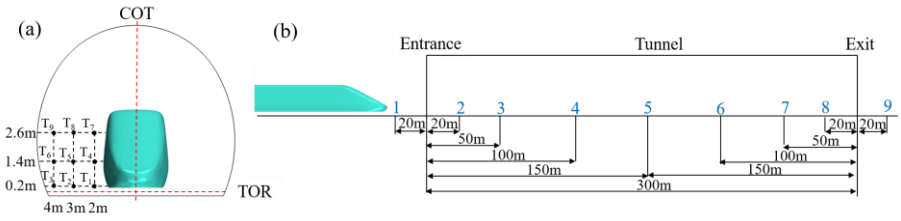

Fig. 8. Distribution of slipstream measurement points: (a) positions of the measurement points relative to the center of track (COT) and top of rail (TOR), and (b) distribution of the cross-section in the tunnel.

A series of slipstream measurement points were arranged in the tunnel to assess the slipstream effect when a train passes through a tunnel, as shown in Fig. 8. Slipstream measuring points were also arranged outside the tunnel entrance and exit to compare and analyze the changes in slipstream at the measuring points outside and inside the tunnel. Because the flow fields on the left and right sides of the train are symmetrical when the train passes through a single-track tunnel, slipstream measuring points were only arranged on one side of the train and the longitudinal distribution of the slipstream monitoring points is presented in Fig. 8(b). The monitoring points were arranged on nine sections, and nine slipstream monitoring points were set on each section. The transverse position and height of the slipstream monitoring points were based on the CEN European Standard (2009).

2.5 Data processing

To facilitate data comparison and analysis, dimensionless processing was conducted for slipstream data, which was defined as follows:

$$U = \frac{u}{V_{train}}, \tag{2}$$

$$V = \frac{v}{V_{train}}, \tag{3}$$

$$W = \frac{w}{V_{train}}, \tag{4}$$

$$U_R = \frac{\sqrt{u^2+v^2+w^2}}{V_{train}}, \tag{5}$$

where u, v, and w are the longitudinal, transverse, and vertical components of the slipstream velocities, respectively, and U, V, and W are the longitudinal, transverse, and vertical components of the non-dimensional slipstream velocities, respectively. V_{train} represents the train speed, which is 350 km/h or 97.22 m/s, and U_R is the non-dimensional resultant slipstream velocity.

2.6 Algorithm Verification

The aerodynamic full-scale test results of the CRH2G high-speed electric multiple units of the Lanxin high-speed railway in operation between Urumqi and Hami were considered to verify the applicability and accuracy of the numerical simulation method adopted in this study. The test tunnel was the Hongxi tunnel, with an effective cross-sectional area of 100 m^2 and a length of 1356 m. The train speed was 250 km/h. The slipstream monitoring points were arranged 120 m from the tunnel exit.

The same calculation model as in the full-scale test was established, and the numerical calculation of the full-scale test model was carried out using the calculation method and medium-scale grid generation strategy of this study. Figure 9 compares the slipstream results obtained from the full-scale test and numerical simulation. The results reveal that the variation law and peak value of the slipstream curves obtained by the experimental test and numerical calculation show a high consistency (i.e., the results of the two are in good agreement, and the error of maximum and minimum values of slipstream speed is within 5%). In this study, the numerical simulation method employed is reliable and can accurately predict the flow in a tunnel.

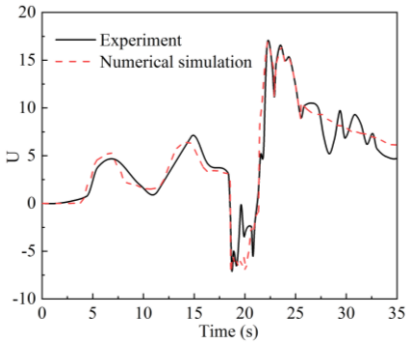

Fig. 9. Slipstream comparison between experimental and numerical results.

3. RESULTS AND DISCUSSION

3.1 Train–Tunnel Aerodynamic Characteristics

In this section, the wake characteristics and slipstream distribution characteristics of high-speed trains passing through tunnels are discussed.

3.1.1 Flow structure analysis

To study the wake structure generated by a train passing through a tunnel, this section analyzes the wake vortex structure at four different moments when the train model with a streamlined nose length of 7 m is passing through the tunnel. The four moments are as follows: when the train has partially entered the tunnel (t_1 = 0.1 s), completely entered the

tunnel (t_2 = 0.25 s), partially exited the tunnel (t_3 = 0.4 s), and completely exited the tunnel (t_4 = 0.48 s). The Q iso-surface approach is an effective method of describing the instantaneous flow structure at the tail of a train. The Q iso-surface is defined by the Q criterion, which is given by

$$Q = -\frac{1}{2}\left(\frac{\partial u_i}{\partial x_j} * \frac{\partial u_j}{\partial x_i}\right) = -\frac{1}{2}\left(\overline{S_{ij}} * \overline{S_{ij}} - \overline{\Omega_{ij}} * \overline{\Omega_{ij}}\right) \quad (6)$$

where S_{ij} and Ω_{ij} are the symmetric and antisymmetric parts of the velocity gradient tensor, respectively.

Figure 10 presents Q iso-surface plots at four different moments when the train runs in the tunnel. Figures 10(a) and (b) show the top and front views. As shown in Fig. 10(a), when the train tail has not entered the tunnel (at t_1), the wake vortex structure of the train is composed of two main vortices, V-1 and V-2, and these vortices have apparent boundaries and do not interfere with each other. Compared with t_1, after the train completely enters the tunnel (at t_2), the flow field at the tail of the train becomes complicated, and the intensity of the wake vortex structure and number of small-scale vortex structures is greater, with V-1 and V-2 blending and ceasing to be apparent. Figure 10(b) shows that the wake vortex is higher when the train is completely in the tunnel (at t_2) than that when the train has not completely entered the tunnel. The aforementioned analysis shows that the wake flow dynamics and slipstream were influenced by the piston effect induced by the train passing through the tunnel. The piston effect increases the tail of the train vortex, making the airflow more chaotic and turbulence more intense.

Although the vortex structure on the tail of the train is complicated, the width and height of the vortex are reduced when the train has partially exited the tunnel (at t_3) compared with those when the train is completely in the tunnel (at t_2). This phenomenon occurs because the intensity of turbulence in the flow field around the train is weakened when only a part of the train runs in the tunnel. After the train completely exits the tunnel (at t_4), the vortex distribution is different from those at the other moments, indicating that many vortices overflow outside the exit of the tunnel, and the vortex height at the exit of the tunnel is almost the same as the height of the tunnel. This behavior is due to a large amount of air being carried out of the tunnel by the train as it exits. In addition, when the train leaves the tunnel completely and runs in open air, the strength of the train wake vortex is weakened; two main vortices are clearly visible, and small-scale vortex structure becomes smaller, similar to the wake structure at t_1. This finding indicates that the wake flow is restricted to a limited space when the train runs in a tunnel, resulting in chaotic flow at the tail of the train, high turbulence, and the formation of more small-scale vortex structures.

Figure 11 shows the instantaneous vorticity amplitude ω distribution when the train passes through the tunnel. In Fig. 11(a), it can be observed that the flow structure around the train when the train passes into the tunnel, particularly in the wake of the train, is

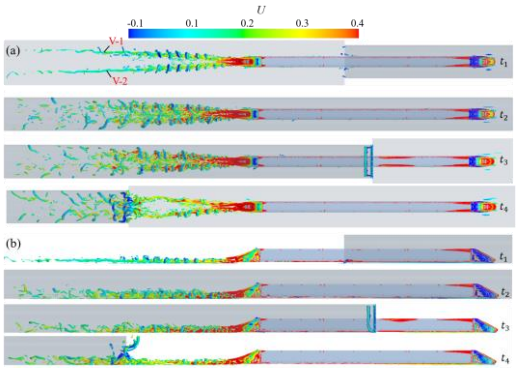

Fig. 10. Instantaneous Q iso-surface (Q = 50,000) plot of train at different moments: (a) top view and (b) side view.

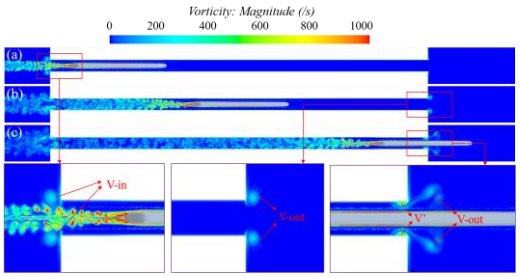

Fig. 11. Instantaneous vortex amplitude ω plot of the train when it (a) enters the tunnel at t = 0.15 s, (b) reaches the middle of the tunnel at t = 0.25 s, and (c) leaves the tunnel at t = 0.4 s.

very complicated. There are two distinct vortices at the tunnel entrance (V-in), which are caused by the airflow into the tunnel when the train enters it. Figure 11(b) shows that the vortex structure at the tunnel entrance diffuses to both sides of the tunnel when the train crosses the middle of the tunnel. Figure 11(b) indicates that there are two V-out vortices at the exit of the tunnel, which are caused by the sudden expansion of space at the tunnel exit while the train is squeezing the air in the tunnel forward. Figure 11(c) shows that V-out is further strengthened and diffused outward when the train leaves the tunnel and passes through the tunnel exit. In addition, two small vortices V' are generated near the tunnel exit, and the vortex here corresponds to the vortex structure at the tunnel exit at t_3 in Fig. 11.

3.1.2 Slipstream Analysis

Except for the difference in the wake flow dynamics, the differences in spatial and temporal distributions of airflow velocity around the train between the open air and inside the tunnel are apparent. First, we compared and analyzed the time histories of the slipstream at monitored points in open air and inside the tunnel. The monitored point in open air outside the tunnel was located 20, 1.4, and 3 m away from the entrance of the tunnel, TOR, and COT, respectively. The monitored point in the tunnel was located 100, 1.4, and 3 m from the entrance of the tunnel, TOR, and Cot, respectively. Figure 12 presents the slipstream time–history curves at the aforementioned two monitored points. In Fig. 12, N and T represent

the moment when the noses of the head and tail cars pass through the monitored points, respectively. In the figure, the distribution and amplitude of the slipstream are significantly different between the monitored points in the open air and the tunnel. The peak value of the slipstream in the tunnel is 0.31, which is larger than that outside the tunnel (0.15), due to the influence of the piston effect of the tunnel. In addition, the slipstream inside or outside the tunnel is affected by the passing of the train. After the train passes, the slipstream considerably fluctuates and reaches its maximum value because of the influence of the train wake (Bell *et al*. 2016; Chen *et al*. 2021c; Li *et al*. 2019). The slipstream at the monitored point of the tunnel is affected by the pressure wave and begins to rise gradually before the train arrives (Fu *et al*. 2017). Figure 12 also indicates that a large backflow is formed at the monitored points in the tunnel during the times at which the head and tail cars pass through the monitored points.

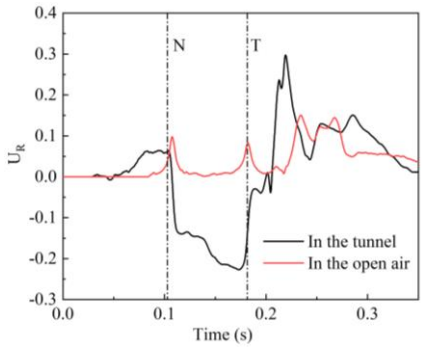

Fig. 12. Comparison of time–history curves of slipstream variation at monitored points in open air and a tunnel.

Figure 12 shows the time variation of the slipstream. In addition, the spatial distribution of the slipstream will be discussed. Figure 13 presents a cloud diagram of the velocity distribution at cross-sections of different positions in the tunnel, whereas Fig. 14 illustrates the time–history curve of slipstream at monitored points at different positions, 100 m away from the entrance of the tunnel. Figure 14(a) presents the time–history curves of slipstream at monitored points of different heights, 3 m away from the COT. Based on Fig. 14(a), the positive peak value of the slipstream decreases with the increasing height from the TOR, mainly because the intensity of the train wake vortex decreases with increasing vertical distance from the TOR. In Fig. 13, the intensity of the train wake vortex gradually weakens, and the velocity amplitude shrinks as the distance from the TOR increases. Therefore, the slipstream amplitude at monitored point T2 is the largest, followed by T5 and T8, as T2 is completely within the influence range of the high-intensity train wake. T8 is separated from the influence area of high-intensity train wake; thus, the slipstream amplitude at this monitored point is the smallest. The curve fluctuation is still large even after the slipstream reaches the maximum value.

Figure 14(b) shows the slipstream time history curves at monitored points with different transverse

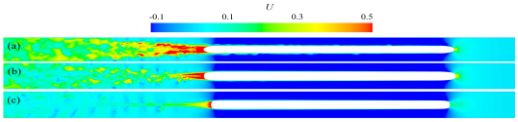

Fig. 13. Velocity distributions in different horizontal planes: (a) 0.2, (b) 1.4, and (c) 2.6 m away from TOR.

spacings 0.2 m away from the TOP. Based on the plot, the slipstream peak value decreases with the increase in the distance between the monitored point and train. This trend occurs because the intensity of the train wake vortex gradually weakens as the distance from the train increases. In Fig. 13(a), the flow field near the train is greatly disturbed, and the velocity pulsation is also large, which is significantly affected by the wake. As a result, the maximum slipstreams at T1, T2, and T3 successively decrease.

Figure 15(a) presents the time history curves of the slipstream at monitored point T2 of sections 20, 100, and 150 m away from the entrance of the tunnel to understand the distribution of the slipstream along the tunnel length. The distributions of the maximum and minimum slipstream speeds at monitored points T2 at sections along the tunnel length are presented in Fig. 15(b). Figure 15(a) indicates that the variation trends of the slipstream time history curves at different monitored points in the tunnel length direction are similar. However, there are significant differences in the slipstream distributions at different monitored points due to the different times at which the

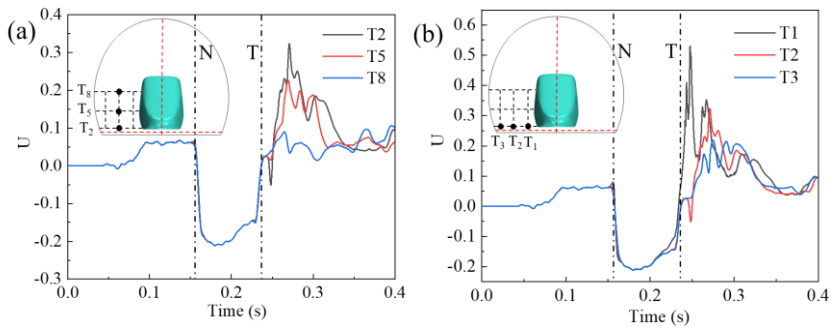

Fig. 14. Slipstream distribution at section 100 m from tunnel entrance: (a) 3 m away from COT and (b) 0.2 m away from TOR.

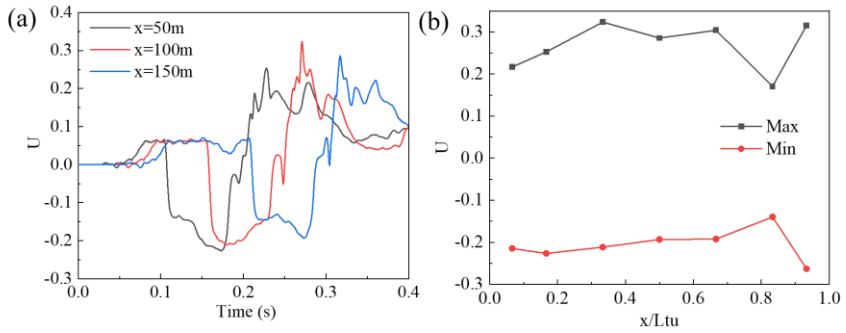

Fig. 15. Slipstream distribution along the tunnel length: (a) slipstream time history curves at monitored points 50, 100, and 150 m away from the tunnel entrance, and (b) distribution of positive and negative peak values of the slipstream.

train passes through the monitored points, different propagation characteristics of the pressure wave, and flow fields around the different monitored points. These are mainly reflected in the differences in the slipstream amplitude and attenuation trend after the train leaves the monitored point.

In addition, based on Fig. 15(a), the slipstream began to fluctuate before the train arrived at the monitored point. This fluctuation was induced by the back-and-forth reflections of the pressure wave generated when the train enters the tunnel, indicating that the propagation of the pressure wave had an impact on the slipstream. Figure 15(b) indicates that the distribution of the slipstream along the tunnel length was not constant. The maximum positive and negative peaks of the slipstream at different positions along the tunnel length were located at the exit of the tunnel. This phenomenon can be explained by Fig. 10. The intensity of the train wake vortex gradually increases and reaches a maximum when the train enters the tunnel from the open air and is in the middle of the tunnel. Therefore, the positive peak value of the slipstream at the monitored point in the middle of the tunnel is also large. As the train leaves the tunnel, the intensity of the trailing vortex in the tunnel begins to weaken. However, when the train completely exits the tunnel, the vortex intensity near the tunnel exit suddenly increases; thus, the positive and negative peak values of the slipstream at the tunnel exit reach their maxima. Along the tunnel length direction, the maximum positive peak of the slipstream is 0.32, which is 45.5% higher than the minimum positive peak. The maximum value of the slipstream negative peak is 0.26, which is 85.7% larger than the minimum negative peak value.

3.2 Comparison of Aerodynamic Characteristics for Different Streamlined Nose Lengths

This section compares and analyzes the effects of the streamlined nose length on the wake vortex structure and slipstream distribution when a high-speed train passes through a tunnel. The streamlined nose length was set to 5, 7, and 9 m.

3.2.1 Instantaneous flow structures

Figure 16 shows the instantaneous Q contour map (Q = 50,000) around the trains with different streamline lengths, colored with dimensionless speed *U*. The flow field in the train wake area of the tunnel is complex. The shorter the nose streamlined length, the more disordered the wake and the greater the vortex intensity. The wake region contains vortices of various sizes, and the vortex structure is composed of two main vortices alongside some small-scale vortices. The wake vortex is generated from the intersection of the streamline and non-streamline at the rear car; then, it converges at the nose of the rear car and continuously falls off and ruptures to the rear in the form of rotary motion. The vortex structure at the tail varies when trains with different nose streamlined lengths pass through the tunnel. It can be seen from the top view that the vortex attached to the streamline area of the tail car falls off, and the two main vortices form in the near wake area (area A). The two main vortex structures become clear as the nose streamlined length increases. The vortices in this area are blended and mixed with each other when the nose streamlined length is 5 m. Conversely, when the nose streamlined length is 7 m, the two main vortices in this region begin to separate. Two separate main vortices can be seen in this area when the nose streamlined length is 9 m.

The width and height of the wake vortex were marked at the four train widths from the nose of the tail car to compare the intensity and influence range of the wake vortex of three nose streamlined lengths trains. In the figure, the nose streamlined length increases from 5 to 9 m, the widths of the wake vortex are 2.17*W*, 1.67*W*, and 1.17*W*, respectively, and the heights are 0.79*H*, 0.64*H*, and 0.3*H*, respectively. This shows that the longer the nose streamlined length, the smaller the width and height of the wake vortex and the narrower the influence range of the wake vortex. This tendency exists because the two main vortices near the wake with a short nose streamlined length are not apparent, and the vortices in the wake area fluctuate unsteadily and break into small-scale vortex structures to diffuse to both sides of the tunnel, widening the wake vortex range. For a train with a long nose streamlined length, the two main vortices at the tail are clearly separated and remain stable for a long time such that they can be tightened over a long propagation distance and spread in a narrow range. Based on Fig. 16, the longer the nose streamlined length, the more uniform the flow field between the streamline and non-streamline of the tail

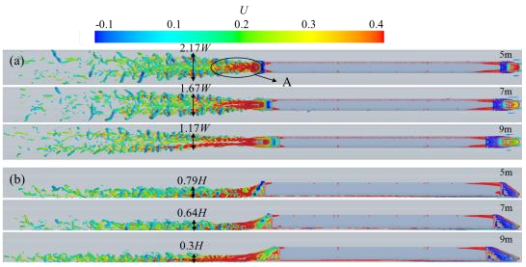

Fig. 16. Instantaneous Q contour map (Q = 50,000) around the train for different streamlined lengths at t = 0.25 s: (a) top view and (b) front view.

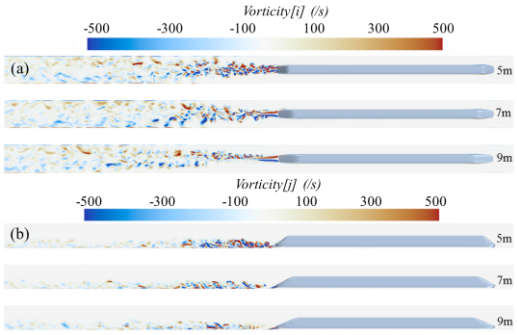

Fig. 17. Comparison of instantaneous vorticity for different streamlined lengths: (a) instantaneous x-vorticity (w_x) in the horizontal plane 0.2 m from the rail surface, and (b) instantaneous y-vorticity (w_y) in the longitudinal section y = 0 m.

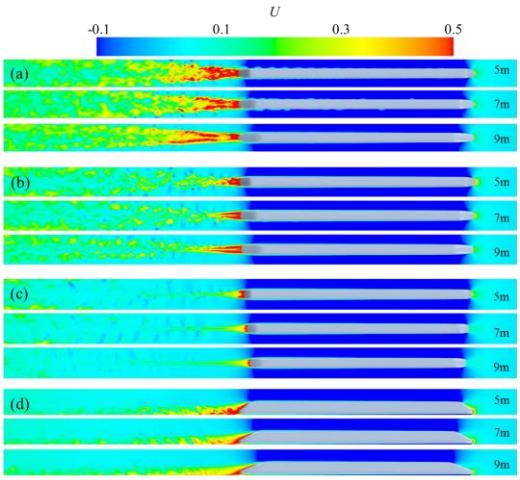

Fig. 18. Comparison of velocity distribution under different nose streamlined lengths at t = 0.25 s: horizontal plane (a) 0.2, (b) 1.4, and (c) 2.6 m from the TOR, and (d) y = 0 m longitudinal section.

car and the smaller the fluctuation of the velocity field in this area. With increasing nose streamlined length, the flow in the wake area is smoother, and the strength of the wake vortex decreases. The difference in the flow structures around the train causes a difference in the slipstream when a train passes through the tunnel.

Figure 17 presents the instantaneous vorticity distribution when the train reaches the middle position of the tunnel. The vortex structure within the wake region of the train is complex, and the two main vortices on both sides of the train tail continue to develop to the rear of the train by rotating in opposite directions.

Based on Fig. 17, there are significant differences in the vorticity distributions in the wake regions of the three different nose streamlined length trains. Compared with the other two nose streamlined lengths, the flow field in the wake region of the train with a nose streamlined length of 5 m is the most chaotic. The intensity and influence scope of the wake vortex are the largest, followed by those of the train with a nose streamlined length of 7 m. The vortex intensity and influence range in the wake area are the smallest when the nose streamlined length of the train is 9 m. Simultaneously, the nose streamlined length affects the development of the vortex near the nose of the tail car. The larger the nose streamlined length, the weaker is the vortex intensity in this area and the more apparent are the two main vortices. Note that although a shorter nose streamlined length leads to stronger wake disturbance, it also means that the energy of the small-scale vortex is dissipated faster, resulting in the rapid breaking of the small-scale vortex in the wake area and a short backward propagation distance of the wake vortex.

3.2.2 Slipstream Analysis

The slipstream fluctuates continuously with time and three-dimensional space due to the influence of the pressure wave, train passing, and train wake when a train runs in a tunnel at a high speed. There are apparent differences in the wake flow structure with different nose streamlined lengths, resulting in considerable differences in the temporal and spatial distributions of slipstream. Figure 18 shows the instantaneous velocity field distributions of different cross-sections when trains with different nose streamlined lengths pass through a tunnel. Figures 18(a)–(c) present the velocity distributions of the horizontal plane 0.2, 1.4, and 2.6 m away from the TOR, respectively, and Fig. 18(d) illustrates the velocity distribution of the longitudinal section y = 0 at the center of the tunnel. Note that the range of the high-velocity train slipstream in the wake region decreases as the nose streamlined length in the tunnel width direction increases but increases as the nose streamlined length in the length direction increases. This behavior occurs because the slipstream affected by the train wake depends on the influence scope and strength of the wake vortex structure. Based on Figs. 16 and 17, a train with a short nose streamlined length has a high-strength wake structure, and the influence range on the tunnel width direction is large. When the nose streamlined length is long, the strength of the train wake vortex is small, and the influence range on the length direction of the tunnel is large. Moreover, based on the figure, the slipstream at the rear of the train gradually decreases as the distance from the TOR increases. Based on Fig. 18(c), the horizontal plane is 2.6 m away from the TOR, the nose stream-

lined length has little effect on the velocity distribution of the wake area. It can also be noticed from Fig. 18(d) that the area with a large slipstream velocity behind the train decreases as the nose streamlined length increases.

Figure 19 shows the slipstream time-history curve of the T2 monitoring point 100 m from the tunnel entrance when trains with different nose streamlined lengths pass through the tunnel. Before the tail nose of the train reaches monitoring point T2, the slipstream curves at the T2 monitoring point for different working conditions coincide. Therefore, the negative peak value of the slipstream is the same for different nose streamlined lengths. The slipstream time history curves under different nose streamlined lengths begin to differ when the tail car passes through monitoring point T2. These differences are mainly caused by the wake difference after the train passes through the monitoring point. The results show that the influence of nose streamlined length on the slipstream is mainly caused by the different wake flow structures at the rear of the train. Based on the figure, the positive peak value of the slipstream decreases as the nose streamlined length increases. The longer the nose streamlined length, the later the positive peak of the slipstream appears. This phenomenon can be explained by Fig. 18(a), where the shorter the nose streamlined length, the more intense is the velocity field pulsation in the wake area, and the closer the area with the maximum velocity is to the nose of the tail car.

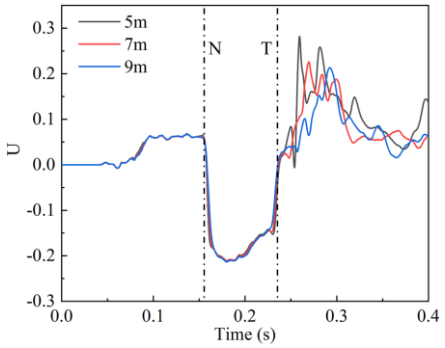

Fig. 19. Slipstream time history curve at T2 measuring point at 100 m from the tunnel entrance under different nose streamlined lengths.

To show the influence of nose streamlined length on the slipstream peak more intuitively, Fig. 20 compares and analyzes the slipstream peak at different monitoring points (T4, T5, and T6) 100 m from the entrance of the tunnel and 1.4 m from the TOR when trains with different nose streamlined lengths pass through the tunnel, where U_{max} represents the positive peak value of the slipstream. Based on the figure, when the nose streamlined length increases from 5 to 9 m, U_{max} exhibits an apparent downward trend, and the closer to the monitoring point of the train, the greater the slipstream drop. U_{max} decreases by 46.6%, 24.5%, and 16.8% when the distance between the monitoring point and tunnel centerline is 2, 3, and 4 m, respectively, indicating that the nose streamlined length has a significant impact on the slipstream in the area close to the train.

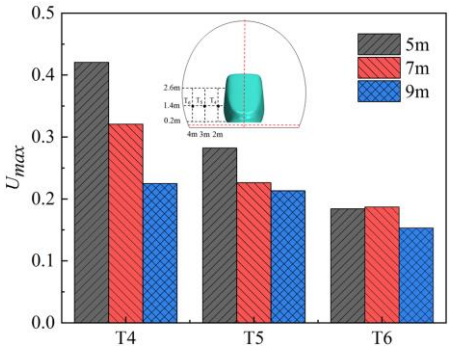

Fig. 20. Comparison of slipstream peaks for different nose streamlined lengths at 100 m from the tunnel entrance.

4. CONCLUSION

In this study, numerical simulation was used to examine the flow structure around a train and the distribution characteristics of the slipstream when it passes through a tunnel at a high speed. Then, the effects of the nose streamlined length of the train on the wake vortex structure and slipstream were compared and analyzed. The conclusions of the study are as follows:

(1) The wake flow fields are vastly different when the train is at different positions in the tunnel due to the influence of the piston effect of the train passing through the tunnel on the wake. In comparison to the situation in which the train is partially or completely outside the tunnel, the wake flow is more disordered, the wake vortex intensity is greater, and there are more small-scale vortex structures when the train is completely running in the tunnel. Numerous vortex structures are generated near the tunnel exit when the train leaves the tunnel.

(2) The slipstream in the tunnel changes slowly under the influence of the pressure wave. The slipstream drops rapidly to a negative value at the time the train passes through the measuring point. After the train passes, it continues to pulsate and reaches its maximum under the influence of the wake. The farther away from the top of the rail and center of the track, the smaller is the influence of the wake and the velocity pulsation of the flow field and slipstream velocity. The distribution of the slipstream along the length of the tunnel is unsteady. Both positive and negative peak values of the slipstream emerge at the tunnel exit.

(3) The shorter the nose streamlined length of the train, the more disordered the wake flow, the greater the vortex intensity, and the greater the influence range of the wake vortex. The longer the nose streamlined length, the more apparent the two main vortices are at the tail of the train and the more uniform the flow field between the streamlined and non-streamlined of the tail car. The larger range of slipstream in the train wake area decreases as the nose

streamlined length in the tunnel width direction increases and increases as the nose streamlined length in the length direction increases. The longer the nose streamlined length, the smaller is the positive peak value of the slipstream, and the later the positive peak of the slipstream appears. The positive peak value of the slipstream U_{max} at monitoring points T4, T5, and T6 at 100 m from the tunnel entrance and 1.4 m from the top of the rail decrease by 46.6%, 24.5%, and 16.8%, respectively, when the nose streamlined length increases from 5 to 9 m.

ACKNOWLEDGEMENTS

The authors would like to acknowledge the computing resources provided by the Key Laboratory of Traffic Safety on Track for academic research.

This research was supported by Fundamental Research Funds for the Central Universities of Central South University (Grant No. 2019zzts266) and the Key R&D Project in Sichuan Province (Grant No. 2019YFG0040).

REFERENCES

Bell, J. R., D. Burton, M. Thompson, A. Herbst and J. Sheridan (2015). Wind tunnel analysis of the slipstream and wake of a high-speed train. *Journal of Wind Engineering and Industrial Aerodynamics* 136, 127-137.

Bell, J. R., D. Burton, M. Thompson, A. Herbst and J. Sheridan (2017). The effect of tail geometry on the slipstream and unsteady wake structure of high-speed trains. Experimental Thermal and Fluid Science 83, 215–230.

Bell, J. R., D. Burton, M. Thompson, A. Herbst and J. Sheridan (2016). Dynamics of trailing vortices in the wake of a generic high-speed train. Journal of Fluids & Structures 65, 238–256.

CEN European Standard (2010). CEN EN 14067-5 Railway Applications - Aerodynamics- Part5: Requirements and Test Procedures for Aerodynamics in Tunnels. CEN.

CEN European Standard (2009). CEN EN 14067-4 Railway Applications - Aerodynamics, Part 4: Requirements and test procedures for aerodynamics on open track. CEN.

Chen, G., X. B. Li and X. F. Liang (2021a). IDDES simulation of the performance and wake dynamics of the wind turbines under different turbulent inflow conditions. *Energy* 238, 121772.

Chen, G., X. B. Li, Z. Liu, D. Zhou, Z. Wang, X. F. Liang and S. Krajnovic (2019). Dynamic analysis of the effect of nose length on train aerodynamic performance. *Journal of Wind Engineering and Industrial Aerodynamics* 184, 198-208.

Chen, G., X. F. Liang and X. B. Li (2022). Modelling of wake dynamics and instabilities of a floating horizontal-axis wind turbine under surge motion. *Energy* 239, 122110.

Chen, G., X. F. Liang, X. B. Li, D. Zhou and F. Lien Sang (2021b). Numerical investigation of vortex induced vibration effects on the heat transfer for various aspect ratios ellipse cylinder. *International Journal of Thermal Sciences* 170, 107138.

Chen, G., X. F. Liang, X. B. Li, D. Zhou, F. Lien Sang and J. Wang (2021c). Dynamic analysis of the effect of platoon configuration on train aerodynamic performance. *Journal of Wind Engineering and Industrial Aerodynamics* 211, 104564.

Chen, X. D., T. H. Liu, X. S. Zhou, W. Li, Hui, T. Z. Xie and Z. W. Chen (2017). Analysis of the aerodynamic effects of different nose lengths on two trains intersecting in a tunnel at 350 km/h. *Tunnelling and Underground Space Technology* 66, 77-90.

Chen, Z., T. Liu, Z. Jiang, Z. Guo and J. Zhang (2018). Comparative analysis of the effect of different nose lengths on train aerodynamic performance under crosswind. Journal of Fluids & Structures 78, 69-85.

Choi, J. K. and K. H. Kim (2014). Effects of nose shape and tunnel cross-sectional area on aerodynamic drag of train traveling in tunnels. *Tunnelling and Underground Space Technology incorporating Trenchless Technology Research* 41, 62–73.

Doi, T., T. Ogawa, T. Masubuchi and J. Kaku (2010). Development of an experimental facility for measuring pressure waves generated by high-speed trains. *Journal of Wind Engineering and Industrial Aerodynamics* 98(1), 55-61.

Flynn, D., H. Hemida and C. Baker (2016). On the effect of crosswinds on the slipstream of a freight train and associated effects. *Journal of Wind Engineering & Industrial Aerodynamics* 156, 14-28.

Fu, M., P. Li and X. F. Liang (2017). Numerical analysis of the slipstream development around a high-speed train in a double-track tunnel. *PLoS One* 12, 1–15.

Gilbert, T., C. J. Baker and A. Quinn (2013). Gusts caused by high-speed trains in confined spaces and tunnels. *Journal of Wind Engineering & Industrial Aerodynamics* 121, 39–48.

Hemida, H. and S. Krajnović (2010). LES study of the influence of the nose shape and yaw angles on flow structures around trains. *Journal of Wind Engineering & Industrial Aerodynamics* 98(1), 34-46.

Hemida, H. and S. Krajnović (2008). LES study of the influence of a train-nose shape on the flow structures under cross-wind conditions. *Journal of Fluids Engineering* 130(9), 253-257.

Ito, M. (2000). Improvement to the aerodynamic characteristics of Shinkansen rolling stock. Proceedings of the Institution of Mechanical Engineers, Part F: *Journal of Rail and Rapid Transit* 214(3), 135-143.

Jiang, Z., T. Liu, X. Chen, W. Li, Z. Guo and J. Niu (2019). Numerical prediction of the slipstream caused by the trains with different marshalling forms entering a tunnel. *Journal of Wind Engineering and Industrial Aerodynamics* 189, 276-288.

Krajnović, S. (2009). Shape optimization of high-speed trains for improved aerodynamic performance. Proceedings of the Institution of Mechanical Engineers, Part F: *Journal of Rail and Rapid Transit* 223(5) 439-452.

Ku, Y. C., J. H. Rho, S. H. Yun, M. H. Kwak, K. H. Kim, H. B. Kwon and D. H. Lee (2010). Optimal cross-sectional area distribution of a high-speed train nose to minimize the tunnel micropressure wave. *Structural and Multidisciplinary Optimization* 42(6), 965-976.

Kwak, M., S. Yun, Y. Lee, H. Kwon, K. Kim and D. H. Lee, (2013). Optimum nose shape of a front-rear symmetric train for the reduction of the total aerodynamic drag. *Journal of Mechanical Science and Technology* 27(12), 3733-3743.

Kwon, H. B., K. H. Jang, Y. S. Kim, K. J. Yee and D. H. Lee (2001). Nose shape optimization of high-speed train for minimization of tunnel sonic boom. *JSME International Journal Series C Mechanical Systems, Machine Elements and Manufacturing* 44(3), 890-899.

Lee, J. and J. Kim (2008). Approximate optimization of high-speed train nose shape for reducing micropressure wave. *Structural and Multidisciplinary Optimization* 35(1), 79–87.

Lee, J. and J. Kim (2007). Kriging-based approximate optimization of high-speed train nose shape for reducing micropressure wave. Proceedings of the Institution of Mechanical Engineers, Part F: *Journal of Rail and Rapid Transit* 221(2), 263-270.

Li, R., P. Xu, Y. Peng and P. Ji (2016). Multi-objective optimization of a high-speed train head based on the FFD method. *Journal of Wind Engineering and Industrial Aerodynamics* 152, 41-49.

Li, X., G. Chen, D. Zhou and Z. Chen (2019). Impact of different nose lengths on flow-field structure around a high-speed train. *Applied Sciences* 9(21), 4573.

Li, X. B., G. Chen, Z. Wang, X. H. Xiong, X. F. Liang and J. Yin (2019). Dynamic analysis of the flow fields around single- and double-unit trains. *Journal of Wind Engineering and Industrial Aerodynamics* 188, 136-150.

Liang, X., G. Chen, X. Li and D. Zhou (2020). Numerical simulation of pressure transients caused by high-speed train passage through a railway station. *Building and Environment* 184, 107228.

Liang, X. F., X. B. Li, G. Chen, B. Sun, Z. Wang, X. H. Xiong, J. Yin,M. Z. Tang, X. L. Li, and S. Krajnović (2020). On the aerodynamic loads when a high speed train passes under an overhead bridge. *Journal of Wind Engineering and Industrial Aerodynamics* 202, 104208.

Liu, Z., G. Chen, D. Zhou, Z. Wang and Z. Guo (2020). Numerical investigation of the pressure and friction resistance of a high-speed subway train based on an overset mesh method. Proceedings of the Institution of Mechanical Engineers, Part F: *Journal of Rail and Rapid Transit* 235(5), 598-615.

Meng, S., X. Li, G. Chen, D. Zhou, Z. Chen and S. Krajnovic (2021a). Numerical simulation of slipstreams and wake flows of trains with different nose lengths passing through a tunnel. *Tunnelling and Underground Space Technology* 108, 103701.

Meng, S., D. Zhou, X. Xiong and G. Chen (2022). The effect of the nose length on the aerodynamics of a high-speed train passing through a noise barrier. *Flow, Turbulence and Combustion* 108(2), 411-431.

Meng, S., S. Meng, F. Wu, X. Li and D. Zhou (2021b). Comparative analysis of the slipstream of different nose lengths on two trains passing each other. *Journal of Wind Engineering and Industrial Aerodynamics* 208, 104457.

Miyachi, T., M. Iida, T. Fukuda and T. Arai (2016). Nondimensional maximum pressure gradient of tunnel compression waves generated by offset running axisymmetric trains. *Journal of Wind Engineering and Industrial Aerodynamics* 157, 23-35.

Muñoz-Paniagua, J., J. García and A. Crespo (2014). Genetically aerodynamic optimization of the nose shape of a high-speed train entering a tunnel. *Journal of wind engineering and industrial aerodynamics* 130, 48-61.

Muñoz-Paniagua, J., J. García, A. Crespo and S. Krajnovic (2012). Aerodynamic optimization of the ICE 2 high-speed train nose using a genetic algorithm and metamodels. *The First International Conference on Railway Technology: Research, Development and Maintenance*.

Munoz-Paniagua, J., J. García, A. Crespo and F. Laspougeas (2015). Aerodynamic optimization of the nose shape of a train using the adjoint method. *Journal of Applied Fluid Mechanics* 8(3), 601-612.

Niu, J., Y. Wang, L. Zhang and Y. Yuan (2018). Numerical analysis of aerodynamic characteristics of high-speed train with different train nose lengths. *International Journal of Heat and Mass Transfer* 127, 188-199.

Paniagua, J. M., J. G. García and A. C. Martínez (2011). Aerodynamic optimization of high-speed trains nose using a genetic algorithm and artificial neural network, In Proceedings of CFD & Optimization 2011. An ECCOMAS Thematic Conference, Antalya, Turkey.

Rocchi, D., G. Tomasini, P. Schito and C. Somaschini (2018). Wind effects induced by high speed train pass-by in open air. *Journal of Wind Engineering and Industrial Aerodynamics* 173, 279-288.

Tian, H. Q., D. Zhou and P. Xu (2006). Aerodynamic performance and streamlined head shape of train. *China Railway Science* 27(3), 47-55.

Wang, J., T. Wang, M. Yang, B. Qian, L. Zhang, X. Tian and F. Shi (2022). Research on the influence of different heating zone lengths on pressure waves and a newly designed method of pressure wave mitigation in railway tunnels. *Tunnelling and Underground Space Technology* 122, 104379.

Xie, T., T. Liu, Z. Chen, W. Li, X. Chen and X. Zhou (2019). Assessment and analysis on variation of trackside pressure induced by trains with different head shapes. *Journal of the China Railway Society* 41(2), 41-49.

Xu, R., F. Wu, M. Zhong, X. Li and J. Ding (2020). Numerical investigation on the aerodynamics and dynamics of a high-speed train passing through a tornado-like vortex. *Journal of Fluids and Structures* 96, 103042.

Yao, S. B., D. L. Guo, Z. X. Sun, G. W. Yang and D. W. Chen (2014). Optimization design for aerodynamic elements of high speed trains. *Com-puters & Fluids* 95, 56-73.

Yao, S. B., D. L. Guo, Z. X. Sun, D. W. Chen and G. W. Yang, (2016). Parametric design and optimization of high speed train nose. *Optimization and Engineering* 17(3), 605-630.

Yoon, T. S., S. Lee, J. H. Hwang and D. H. Lee (2001). Prediction and validation on the sonic boom by a high-speed train entering a tunnel. *Journal of Sound and vibration* 247(2), 195-211.

Zhang, Z. and D. Zhou (2013). Wind tunnel experiment on aerodynamic characteristic of streamline head of high speed train with different head shapes. *Journal of Central South University (Science and Technology)* 44(6), 2603-2608.